This is a non-peer-reviewed preprint for EarthArXiv. This paper is under review at Remote Sens. Environ.

Diagnosing spatial biases and uncertainties in global fire emissions inventories: Indonesia as regional case study

Tianjia Liu[1], Loretta J. Mickley[2], Miriam E. Marlier[3], Ruth S. DeFries[4], Md Firoz Khan[5], Mohd Talib Latif[6], and Alexandra Karambelas[7]

[1] Department of Earth and Planetary Sciences, Harvard University, Cambridge, MA, USA
[2] School of Engineering and Applied Sciences, Harvard University, Cambridge, MA, USA
[3] RAND Corporation, Santa Monica, CA, USA
[4] Department of Ecology, Evolution, and Environmental Biology, Columbia University, New York, NY, USA
[5] Center for Tropical Climate Change System (IKLIM), Institute of Climate Change, Universiti Kebangsaan Malaysia, Bangi, Selangor, Malaysia
[6] School of Environmental and Natural Resource Sciences, Faculty of Science and Technology, Universiti Kebangsaan Malaysia, Bangi, Selangor, Malaysia
[7] The Earth Institute, Columbia University, New York, NY, USA

*Corresponding Author: Tianjia Liu (tianjialiu@g.harvard.edu)

Keywords: fire emissions, MODIS, burned area, active fires, smoke, Indonesia, Google Earth Engine

Abstract

Models of atmospheric composition rely on fire emissions inventories to reconstruct and project impacts of biomass burning on air quality, public health, climate, ecosystem dynamics, and land-atmosphere exchanges. Many such global inventories use satellite measurements of active fires and/or burned area from the Moderate Resolution Imaging Spectroradiometer (MODIS). However, differences across inventories in the interpretation of satellite imagery, the emissions factors assumed for different components of smoke, and the adjustments made for small and obscured fires can result in large regional differences in fire emissions estimates across inventories. Using Google Earth Engine, we leverage 15 years (2003-2017) of MODIS observations and 6 years (2012-2017) of observations from the higher spatial resolution Visible Imaging Infrared Radiometer Suite (VIIRS) sensor to develop metrics to quantify five major sources of spatial bias or uncertainty in the inventories: (1) primary reliance on active fires versus burned area, (2) cloud/haze burden on the ability of satellites to "see" fires, (3) fragmentation of burned area, (4) roughness in topography, and (5) small fires, which are challenging to detect. Based on all these uncertainties, we devise comprehensive "relative fire confidence scores," mapped globally at 0.25° x 0.25° spatial resolution over 2003-2017.

We then focus on fire activity in Indonesia as a case study to analyze how the choice of a fire emissions inventory affects model estimates of smoke-induced health impacts across Equatorial Asia. We use the adjoint of the GEOS-Chem chemical transport model and apply emissions of particulate organic carbon and black carbon (OC+BC smoke) from five global inventories: Global Fire Emissions Database (GFEDv4s), Fire Inventory from NCAR (FINNv1.5), Global Fire Assimilation System (GFASv1.2), Quick Fire Emissions Dataset (QFEDv2.5r1), and Fire Energetics and Emissions Research (FEERv1.0-G1.2). We find that modeled monthly smoke $PM_{2.5}$ in Singapore from 2003-2016 correlates with observed smoke $PM_{2.5}$, with r ranging from 0.65-0.84 depending on the inventory. However, during the burning

season (July to October) of high fire years (e.g., 2006 and 2015), the magnitude of mean Jul-Oct modeled smoke $PM_{2.5}$ can differ across inventories by more than 20 μg m^{-3}. Using the relative fire confidence metrics, we deduce that uncertainties in this region arise primarily from the small, fragmented fire landscape and very poor satellite observing conditions due to clouds and thick haze at this time of year. Indeed, we find that modeled smoke $PM_{2.5}$ using GFASv1.2, which adjusts for fires obscured by clouds and thick haze and accounts for peatland emissions, is most consistent with observations in Singapore, as well as in Malaysia and Indonesia. Finally, we develop an online app called FIRECAM for end-users of global fire emissions inventories. The app diagnoses differences in emissions among the five inventories and gauges the relative uncertainty associated with satellite-observed fires on a regional basis.

1. Introduction

Models of atmospheric composition depend on global fire emissions inventories to reconstruct and project the impacts of biomass burning on air quality (Cusworth et al., 2018), public health (Crippa et al., 2016; Koplitz et al., 2016), climate (Rogers et al., 2015; Tosca et al., 2013), ecosystem dynamics (Yi et al., 2014), and land-atmosphere exchanges (Prentice et al., 2011). Many regional and global modeling studies consider only one global fire emissions inventory as input (Crippa et al., 2016; Hu et al., 2018; Kim et al., 2015; Koplitz et al., 2016; Maasakkers et al., 2016; Marlier et al., in review) primarily to limit computational cost. User reasons for the choice of inventory include availability (only a few inventories are available in near-real time) and spatio-temporal resolution; some chemical transport models (CTM) impose a specific inventory by default. However, disagreements in the magnitude and temporal variability of emissions among inventories can significantly impact modeled estimates of variables relevant to air quality (Cusworth et al., 2018), public health (Koplitz et al., 2018), or the budgets of atmospheric species (Heymann et al., 2017; Shi et al., 2015; Zhang et al., 2014). Thus, it is important to understand the underlying causes for differences in both the magnitude and spatio-temporal variability of fire emissions in order to better inform fire prediction (Chen et al., 2017), land management decisions (Marlier et al., in review), and other applications. In this work, we identify and quantify potential sources of discrepancies and uncertainties among several global fire emissions inventories.

Five global fire emissions inventories are widely used in modeling studies: (1) Global Fire Emissions Database (GFED; van der Werf et al., 2017), (2) Fire Inventory from NCAR (FINN; Wiedinmyer et al., 2011), (3) Global Fire Assimilation System (GFAS; Kaiser et al., 2012), (4) Quick Fire Emissions Dataset (QFED), and (5) Fire Energetics and Emissions Research (FEER; Ichoku and Ellison, 2014) (Table 1). Estimates of fire emissions generally follow the "bottom-up" (e.g. GFED, FINN) or "top-down" approach (e.g. QFED, GFAS, FEER). The bottom-up burned area approach in GFED and FINN is based on MODIS-derived burned area (MCD64A1) and/or active fires (MOD14, MYD14). Fuel loadings, combustion completeness, and emissions factors, which are dependent on region and land use/land cover (LULC), are then used to convert burned area to fire emissions. Fuel loadings are derived from biogeochemical models (Hoelzemann et al., 2004; van der Werf et al., 2010), and combustion completeness is estimated as a function of soil moisture (van der Werf et al., 2017) or tree cover (Wiedinmyer et al., 2011). Emissions factors are compiled from lab experiments and vary by land use and land cover (Akagi et al., 2011; Andreae and Merlet, 2001). The top-down approach in QFED, GFAS, and FEER uses fire energy from MODIS-derived fire radiative power (FRP), which is remotely sensed at top-of-atmosphere. Fire radiative energy (FRE), or the temporal integral of FRP, approximately linearly scales with the mass of dry matter consumed as fuel due

to combustion (Wooster et al., 2005). Besides correcting for fires obscured by clouds in the top-down approach, GFAS, QFED, and FEER also use MODIS aerosol optical depth (AOD) to determine scaling factors for emissions of organic carbon (OC), black carbon (BC), and particulate matter less than 2.5 μm in diameter ($PM_{2.5}$), which includes OC and BC.

To understand the causes for differences in fire emissions estimates, we first devise five "relative fire confidence metrics" based on major methodological differences between the five global inventories and factors that can affect satellite observing conditions: (1) type of input satellite fire dataset (i.e., burned area versus active fires), (2) cloud/haze obscuration of land surface, (3) burn extent and fragmentation, (4) variance in topography, and (5) additional small fires from VIIRS. We combine the five relative fire confidence metrics to map the relative fire confidence score for bottom-up emissions inventories primarily based on burned area (e.g. GFED) or active fire area (e.g. FINN). For top-down inventories, we estimate an FRP-based score to estimate the potential FRP enhancement from unobserved, primarily small fires and also to account for cloud-gap enhancements that boost emissions in GFAS, QFED, and FEER.

We then focus on Indonesia as a regional case study, as Indonesia can contribute a substantial fraction of annual global fire emissions. By some estimates, fires in Equatorial Asia, which mostly occur in Indonesia, account for 8% of carbon emissions from global fire activity on average, but as much as over a third during high fire years (van der Werf et al., 2017). Three main factors contribute to severe haze episodes over Equatorial Asia: (1) synoptic meteorology, (2) fires used for agricultural management, and (3) carbon-rich peatlands in Indonesia. First, during years with a strong El Niño and positive Indian Ocean Dipole phase, such as 2006 and 2015, suppression of convection over Indonesia leads to drought conditions (Crippa et al., 2016; Fernandes et al., 2017; Koplitz et al., 2016). Chen et al. (2017) found a temporal cascade of pan-tropical fires, including large fires in Indonesia, driven by the El Niño Southern Oscillation (ENSO) and modulated by changes in precipitation and terrestrial water storage. Second, smallholder farms and industrial concessions (oil palm, pulpwood, and rubber) are typically managed by fire to clear residues; forests are also cleared for agriculture and new plantations via burning (Dennis et al., 2005; Marlier et al., 2015). Third, if the water table is low, peat fires can burrow underground and become extremely difficult to extinguish. Such fires can smolder for days to weeks, releasing substantial amounts of greenhouse gases and smoke into the atmosphere (Gras and Jensen, 1999; Hayasaka et al., 2014; Rein et al., 2008; van der Werf et al., 2008).

The high concentrations of $PM_{2.5}$ generated by fires in Equatorial Asia pose adverse health risks, leading to increased short-term and long-term premature mortality. For example, Koplitz et al. (2016), Crippa et al. (2016), and Marlier et al. (in review) estimate 75,600-100,300 long-term premature adult deaths from cardiovascular and respiratory disease in Equatorial Asia due to the 2015 severe haze event. However, each of these studies differ in methodology, and specifically, in the global fire emissions inventory used: GFASv1.0 in Koplitz et al. (2016), FINNv2.0 in Crippa et al. (2016), and GFEDv4s in Marlier et al. (in review). In this study, we diagnose the impact of using different emissions inventories on estimates of population-weighted smoke exposures for Singapore, Indonesia, and Malaysia.

To summarize, we first identify the methodological differences between five global fire emissions inventories and use Google Earth Engine to develop five relative fire confidence metrics to quantify some of the uncertainties. We then isolate the impact of using different inventories to estimate smoke exposure in Equatorial Asia from fires in Indonesia. Finally, we develop an online tool to help end-users to rapidly gauge the regional differences in emissions estimates and reduce potential biases in model results.

2. Methods

2.1 Satellite fire datasets

We leverage Google Earth Engine, a petabyte-scale cloud computing platform, to access, process, and analyze the satellite datasets needed for this study (Gorelick et al., 2017). Google Earth Engine couples an expansive data catalog with cloud computing to make rapid geospatial analysis possible on a global scale. We primarily use the Collection 6 (C6) satellite fire datasets from the MODIS sensors aboard the Terra and Aqua satellites, which have daily overpasses at ~10:30 am/pm and ~1:30 am/pm local time, respectively. These datasets are used in the construction of the five global fire emissions inventories considered here. We analyze 15 years (2003-2017) of data from Collection 6 MCD64A1 burned area at 500 m resolution (Giglio et al., 2018, 2009), MOD/MYD14A1 FRP and fire mask at 1 km resolution (Giglio et al., 2016, 2003), and MCD14ML active fire geolocations also at 1 km resolution. We hereafter refer to the Level-3 gridded active fire products MOD14A1 (Terra) and MYD14A1 (Aqua) collectively as MxD14A1 and Level-2 swath products as MxD14. We also use Collection 1 VNP14IMGML active fire geolocations (375 m resolution), available since 2012, from the VIIRS sensor aboard the Suomi National Polar-orbiting Partnership (S-NPP) satellite with overpasses comparable to those of Aqua.

2.2 Relative fire confidence metrics

We devise five simple fire confidence metrics to assess the overall spatial variability and relative bias in global fire emissions inventories at 0.25° x 0.25° spatial resolution and aggregated across 15 years (2003-2017) from monthly timesteps, as described below. Then, as an example to end-users, we integrate the five metrics into more comprehensive "scores" to independently evaluate the relative spatial variability in uncertainty for bottom-up and top-down inventories.

(1) **Spatial discrepancy between burned area and active fire area:** We classify two main types of bottom-up emissions inventories, based on the observations used to derive these inventories. For example, both GFED and FINN estimate burned area, but GFED uses the MCD64A1 burned area product, and FINN relies on MCD14ML active fire geolocations. MODIS burned area is typically classified based on the difference in the surface reflectance, or Normalized Burn Ratio (NBR), of pre-burn and post-burn images, while MODIS active fires are detected as "hotspots," or thermal anomalies, each of which can be associated with areal extent to estimate burned area. To avoid confusion, we refer to burned area derived from MCD64A1 as $BA_{MCD64A1}$ or burned area (BA; as in GFED) and that from MxD14A1 as $BA_{MxD14A1}$ or "active fire area" (AFA; as in FINN). In contrast to the high threshold for the MCD64A1 burned area product, which reliably classifies burn scars > 1.2 km^2 (Giglio et al., 2006), the MxD14A1 active fire product can detect cool, smoldering fires more consistently and fires as small as 100 m^2 under clear-sky conditions (Giglio et al., 2003). However, burned area products may better capture short-lasting fires and fires obscured by thick haze or clouds since the burned area pre-burn versus post-burn algorithm is not limited by satellite overpass times (Giglio et al., 2009). To gauge the relative areal discrepancy of $BA_{MCD64A1}$ and $BA_{MxD14A1}$, we first aggregate $BA_{MCD64A1}$ to the 1-km spatial resolution of $BA_{MxD14A1}$. We then estimate total $BA_{MCD64A1}$ outside $BA_{MxD14A1}$ (BA_β) and $BA_{MxD14A1}$ outside $BA_{MCD64A1}$ (BA_α), over 2003-2017, and calculate the normalized difference index of BA_β and BA_α at 0.25° x 0.25° spatial resolution:

$$\frac{\Sigma BA_{\beta} - \Sigma BA_{\alpha}}{\Sigma BA_{\beta} + \Sigma BA_{\alpha}} \quad (1)$$

where

$$BA_{\beta} = BA_{MCD64A1} - (BA_{MCD64A1} \cap BA_{MxD14A1}) \quad (2)$$

$$BA_{\alpha} = BA_{MxD14A1} - (BA_{MCD64A1} \cap BA_{MxD14A1}) \quad (3)$$

The range of the normalized difference index (-1 to +1) for the BA-AFA discrepancy indicates whether grid cells are either dominated by burned area (> 0) or active fire area (< 0). If either burned area or active fire area dominates (near -1 or +1), the datasets will not agree, and uncertainty is high. If the index is ~0, the discrepancies between the datasets are minimal, wherein $BA_{\beta} \approx BA_{\alpha}$; in this case, however, the magnitude of BA_{β} and BA_{α} can vary while yielding similar index values.

(2) **Cloud/haze effect on the ability of satellites to "see" fires:** Persistent cloud coverage and thick haze limit the opportunities for satellites to detect active fires or retrieve usable scenes for burned area classification. This metric diagnoses the fractional monthly cloud/haze burden at 500-m spatial resolution, weighted by FRP. We use FRP rather than burned area since FRP is linearly related to dry matter emissions and more readily captures small fires. We use the Collection 6 MODIS daily surface reflectance products MxD09GA and follow the algorithm proposed by Xiang et al. (2013) in each pixel, with "pixel" defined as one satellite observation in the native MODIS sinusoidal projection:

$$\frac{\rho_7 - \rho_1}{\rho_7 + \rho_1} < 0 \quad (4)$$

$$\rho_1 > 0.3 \quad (5)$$

where ρ_i is the surface reflectance of MODIS band i, with ρ_1 indicating the 620-670 nm band (Red) and ρ_7, the 2105-2155 nm band (SWIR-2). Cloudy and hazy pixels tend to be saturated in the visible bands relative to SWIR bands (Xiang et al., 2013). Pixels are classified as cloudy/hazy if either of the two criteria is met (Eq. 4 and 5). We consider only those pixels with one or more active fire or burned area observations over the 2003-2017 timeframe to exclude misclassification of cloud/haze in snow, ice, and desert regions. After averaging the fraction of clouds and haze across 0.25° x 0.25° grid cells, we weight the monthly fractional cloud/haze burden by FRP aggregated by month and satellite, over 2003-2017, to place more emphasis on the observing conditions during the months and hours of the diurnal cycle when fires are more likely to occur.

Like Xiang et al. (2013), MODIS also diagnoses clouds and haze but at coarser, 1-km resolution, which can result in overestimates of the cloud/haze fraction since clear pixels are mixed with cloudy or mixed cloudy pixels. However, the MODIS algorithm is better able than Xiang et al. (2013) to separate clouds or haze from bright surfaces such as snow/ice, desert, and built-up areas. We therefore use the FRP-weighted cloud/haze fraction derived from the MODIS algorithm to identify grid cells that may be misclassified as clouds due to the underlying bright surfaces. We assume that those pixels that MODIS characterizes as "cloudy" or having "mixed" clouds, cloud shadow, or high aerosol content are pixels obscured by cloud or haze. Then, for these grid cells, we check whether the FRP-weighted cloud/haze fraction derived from the Xiang

et al. (2013) algorithm is positive. If yes, we use the FRP-weighted cloud/haze fraction from the MODIS algorithm for our metric.

(3) **Fragmentation and size of contiguous burned area:** Burned area products can better capture large, contiguous fires than small, fragmented fires due to the greater difference in NBR from pre-fire to post-fire and the persistence of burn scars on the land surface. On croplands, the small drop in NBR due to small fires can be conflated with harvest or masked by timely sowing of the next crop or by regrowth (Hall et al., 2016). In contrast, active fire products can generally detect such small, fragmented fires more accurately, so long as they occur during the satellite overpasses and are not obscured by clouds or haze. Dense clusters of small fires within a pixel can also increase the detection probability by enhancing the thermal anomaly or the NBR difference relative to background. For this metric, we estimate the total burned area and number of burn scar fragments over 2003-2017, using the average burned area per contiguous burn scar patch as a proxy for burn scar size and fragmentation. The *connectedComponents* function in GEE allows us to estimate the number of contiguous burn patches on a monthly basis at 500-m spatial resolution. However, since *connectedComponents* limits the maximum number of pixels per patch at 256 pixels, we account for burn scars larger than this as an extra burn scar fragment. The 0.25° x 0.25° grid used to extract the contiguous burn scars sets an upper bound on burned area per patch for those large fires extending across multiple grid cells. Values > 2 km^2 per burn fragment indicate large, contiguous fires, while small values represent small, fragmented fires.

(4) **Roughness in topography:** Rough terrain, or large variances in local elevation, can inhibit active fire detection or burned area classification by introducing shadows, leading to insufficient background control pixels and artificial variations in surface reflectance. We estimate the neighborhood variance of terrain elevation as an indication of rough terrain. We use the Global Multi-resolution Terrain Elevation Data 2010 (GMTED2010) at 7.5 arc seconds (~250 m) spatial resolution, derived primarily from the Shuttle Radar Topography Mission (SRTM) Digital Terrain Elevation Data from the National Geospatial-Intelligence Agency (NGA). For each pixel, we estimate the neighborhood variance using a square kernel with a radius of 2 pixels. We then mask out water bodies using the 250-m MODIS/Terra land/water mask (MOD44W C6) and upscale the topography variance to 0.25° x 0.25° spatial resolution by calculating the mean. Values close to 0 m^2 indicate flat topography, while values > 1000 m^2 indicate rough, mountainous terrain.

(5) **Additional small fires detected by VIIRS:** VIIRS aboard S-NPP detects active fires at 375-m (I-bands) and 750-m (M-bands) spatial resolution in comparison to the 1-km spatial resolution of MODIS active fire detections (Schroeder and Giglio, 2017). The difference in spatial resolution suggests that VIIRS can detect smaller and cooler fires than MODIS. However, global fire emissions inventories have historically depended on MODIS since VIIRS is available only since 2012, or over a decade less than MODIS. While these additional small fires may comprise only a small portion of the global carbon budget, they can be important local point sources that contribute to regional air pollution. We approximate additional FRP observed by VIIRS at 375-m spatial resolution as the fractional FRP of VIIRS fires outside MODIS active fire and burned area pixels during the time period when the two satellite records overlap (2012-2017). Values range from 0 (no additional VIIRS FRP outside MODIS burn extent) to 1 (only VIIRS FRP).

2.2.1 Bottom-up inventories: relative fire confidence scores (BA-score, AFA-score)

Taken together, the five metrics described above capture the primary reliance on MODIS burned area (e.g., GFED) versus active fire (e.g., FINN) products as the base input satellite-derived fire dataset in a bottom-up approach and difficulty in the satellite detection of fires due to

cloud/haze obscuration and limited spatial and temporal resolution. Using these five metrics, we estimate a relative fire confidence score for the two bottom-up emissions inventories, which are based on either burned area (as in GFED) or active fire area (as in FINN). For each metric and each grid cell, we assign an initial integer confidence score ranging from 0 to 10, with 10 as highest confidence score, based on the decile distribution of all grid cells. Grid cells with only MODIS active fire, only MODIS burned area, or only VIIRS active fire observations are assigned the lowest confidence score of 0. We then average the scores from the fire confidence metrics in each grid cell and re-center the scale as the median score for the final relative fire confidence score for that grid cell. This score represents the relative degree to which we can be confident in fire emissions for these inventories. We associate low cloud/haze burden, low variance in elevation, and low fraction of additional VIIRS fires with high confidence. To assess inventories based on burned area (e.g., GFED), we calculate a "BA-score," in which high burned area outside active fire area (metric 1) and low burn fragmentation (metric 3) denote high confidence. For inventories based on active fires (e.g., FINN), we calculate an "AFA-score," in which we reverse the scales for metrics 1 and 3 and place more relative confidence in grid cells dominated by active fire area over burned area and fragmented burn landscapes.

2.2.2 Top-down inventories: adjusted potential FRP adjustment (pFRP)

Top-down FRP-based inventories often include statistical cloud-gap adjustment and/or smoke AOD constraints, making them difficult to directly compare against the bottom-up inventories. These cloud-gap adjustments correct for fires blocked from satellite detection due to clouds or thick haze. We thus devise a separate score, the adjusted potential FRP enhancement (pFRP), or "FRP-score," to assess the three top-down inventories (GFAS, QFED, FEER). The pFRP score diagnoses additional fire energy, unaccounted for by the MODIS active fires product but indicated by large burn scars from the MODIS burned area product or very small fires from the 375-m VIIRS active fires product. We first estimate the potential FRP enhancement as the sum of (1) fractional FRP inside MCD64A1 burned area extent but outside active fire area, over 2003-2017, and (2) fractional VIIRS FRP outside the combined extent of both MODIS burned area and active fire area, or metric 5, over 2012-2017. To obtain the adjusted potential FRP enhancement, we then multiply the potential FRP enhancement by the complement of the cloud/haze obscuration fraction, or metric 2. High pFRP values suggest low confidence in top-down inventories under clear-sky conditions.

2.3 Global fire emissions inventories

To convert burned area or FRP into emissions, fire emission inventories rely on estimates and assumptions regarding an array of variables as land cover type, fuel load, or emissions factors. Here we describe these estimates and assumptions across five inventories (GFEDv4s, FINNv1.5, GFASv1.2, QFEDv2.5r1, and FEERv1.0-G1.2) over 2003-2016 and at both global and regional scale (Table 1). We then compare the resulting emissions of carbon dioxide (CO_2), carbon monoxide (CO), methane (CH_4), organic carbon (OC), black carbon (BC), and fine particulate matter ($PM_{2.5}$) emissions from five global fire emissions inventories. Each inventory is described in more detail in Supplementary Section S2.

2.4 Modeling smoke $PM_{2.5}$ from regional fire emissions

Following Kim et al. (2015) and Koplitz et al. (2016), we use the adjoint of the GEOS-Chem CTM to estimate the influence of upwind fires on smoke exposure at population-weighted receptors. As used here, the GEOS-Chem adjoint maps the sensitivities of smoke $PM_{2.5}$ at

particular receptors to fire emissions in grid cells across a source region, creating a footprint of such sensitivities. These footprints depend on the transport pathways from the source to the receptor and vary with meteorology. By multiplying these sensitivities by the different fire emissions inventories, we can easily compare estimates of monthly smoke $PM_{2.5}$ exposure in Indonesia, Singapore, and Malaysia, from 2003-2016. We thus apply monthly adjoint sensitivities, which span a range of meteorology from 2005-2009, to the sum of OC and BC emissions, the main components of smoke $PM_{2.5}$. Due to the high computational cost of the GEOS-Chem adjoint, we match existing 2005-2009 sensitivities to each emissions year from 2003-2016 by determining the closest meteorological year in terms of rainfall (Kim et al., 2015; Koplitz et al., 2016). To do so, we use daily rainfall rates from Climate Hazards Group Infrared Precipitation with Station Data (CHIRPS; Funk et al., 2015), averaged temporally over the fire season and spatially over Sumatra and Kalimantan, Indonesia (Figure S3). As in Fernandes et al. (2017) and Marlier et al. (in review), we define the fire season in Indonesia as July to October.

Following Marlier et al. (in review), we further validate modeled smoke $PM_{2.5}$ with ground observations in Singapore. We first extend the daily $PM_{2.5}$ observations, available from 2014-2016, from the Singapore National Environment Agency (NEA) to 2010 by converting Pollution Standards Index (PSI) observations to $PM_{2.5}$. To further extend the record back to 2003, we train a multi-variate regression model of monthly mean NEA $PM_{2.5}$ observations using visibility, air temperature, wind speed, and rainfall observations from the Singapore Changi airport, available from NOAA Global Summary of the Day (GSOD). The model yields an adjusted r^2 with observations of 0.94 (Figure S5). We then reconstruct monthly $PM_{2.5}$ for 2003-2016 and subtract the background $PM_{2.5}$, or the median $PM_{2.5}$ (13.77 $\mu g\ m^{-3}$) during non-fire season months (January to June and November to December), to obtain smoke $PM_{2.5}$ for our validation. Validation for Malaysia and Indonesia is described in Supplementary Section S3.2.

4. Results

4.1 Spatial patterns in relative fire confidence metrics and scores

Overall, the five relative fire confidence metrics broadly differentiate: (1) large, continuous versus small, fragmented landscapes, (2) cloudy/hazy versus clear satellite observing conditions during the fire season, and (3) flat versus mountainous or rugged terrain. First, the map of BA-AFA discrepancies (metric 1) reveals the regions where the burned area BA_β and active fire area extent BA_α disagree. Regions dominated by high burned area outside the active fire area extent ($BA_\beta >> BA_\alpha$) include the western Australia shrublands, sub-Saharan Africa savannas, and Kazakhstan and eastern Mongolia grasslands. Regions dominated by active fire area outside burned area extent ($BA_\beta << BA_\alpha$) are more widespread and primarily cover agricultural and/or mountainous areas (Figure 1). Second, the FRP-weighted cloud/haze fraction (metric 2) shows that tropical and boreal forest regions, as well as eastern China, are conducive to poor satellite observing conditions due to cloud or haze during the fire season, with index values greater than 0.5 (Figure 2). These areas with persistent cloud/haze burden are consistent with independent estimates of high mean cloud frequency (Wilson and Jetz, 2016) and are also co-located with high MODIS burn date uncertainty, indicating that many retrieved satellite scenes are unusable (Figure S9). Third, the pattern of burn size and fragmentation (metric 3) is similar to that of the BA-AFA discrepancy: areas with large, contiguous fires are better captured by burned area, while areas with small, fragmented fires are better represented by active fire detections (Figure 3). Our method for burn size/fragmentation yields spatial patterns consistent

with fire size from the Global Fire Atlas, a catalog that characterizes nearly 13.3 million individual fires detected by MODIS (Andela et al., 2018). Fourth, topographical variance (metric 4) differentiates mountainous or rugged terrain, such as in western U.S. and southeast Asia, versus flat terrain, such as in northern India and western Australia (Figure 4). Fifth, the map of VIIRS fires outside the MODIS burn extent (metric 5) reveals locations dominated by small fires that are not well-detected by a coarser resolution sensor like MODIS (Figure 5). In over half of grid cells with MODIS active fire or burned area observations, ~50% of VIIRS FRP is not captured by the MODIS burn extent, revealing the importance of very small fires.

Taken together, the five metrics compose the relative fire confidence scores for bottom-up emissions inventories primarily derived from either burned area (BA-score; Figure S1a), such as GFEDv4s, or active fire area (AFA-score; Figure S1b), such as FINNv1.5. While the mapped BA-score and AFA-score mostly track the patterns of the large, contiguous fires versus small, fragmented fires, some areas exhibit low relative confidence (e.g., eastern China croplands, Democratic Republic of Congo tropical forests) or high relative confidence (e.g., central-southern Amazon forests, southern Africa savannas in Botswana and Namibia) for both scores due to the effects of cloud/haze cover and/or topographical variance. Some caveats apply here. While we take the BA-score to apply to GFEDv4s, this inventory also boosts burned area using active fire counts to account for small fires. Additionally, for AFA-score, we assume an active fire area of 1 km^2 for all fires, while FINNv1.5 uses 0.75 km^2 for savanna and grassland fires. Both inventories primarily depend on outdated MODIS fire products: GFEDv4s uses MCD64A1 C5.1 burned area, and FINNv1.5 uses MCD14ML C5 active fires. For all our metrics, we use updated satellite products from MODIS C6 (MCD64A1 and MxD14A1). Despite our simplified approach and use of different versions of the satellite fire products, the normalized difference between GFEDv4s burned area and FINNv1.5 active fire area is spatially well-correlated with the BA-AFA discrepancy ($r = 0.59$, $p < 0.01$), or metric 1. We also find that the normalized difference between GFEDv4s and FINNv1.5 emissions for all six species is also moderately correlated with the BA-AFA discrepancy ($r = 0.52$-0.57, $p < 0.01$), confirming that the difference between GFEDv4s and FINNv1.5 emissions is related to the satellite fire input dataset used.

The pFRP metric assesses top-down FRP-based emissions inventories (GFAS, QFED, and FEER; Figure S2). In total, we estimate 31% and 38% potential FRP enhancement from large fires (using MODIS BA) and very small fires (using VIIRS FRP), respectively, from 2003-2017. Put another way, the FRP-based inventories may be missing more than two-thirds of fires under clear sky conditions. Regions with low pFRP, and thus high uncertainty, include India and sub-Saharan Africa. In these regions, the low pFRP implies that either the satellite overpasses are missing a large number of short-lived or fast-spreading fires or the fires are too small to detect at coarse resolution. For example, the satellite overpasses at 10:30 am and 1:30 pm likely underestimate fire energy in the sub-tropics, where fire activity generally peak in the late afternoon (Giglio, 2007). Regions characterized by clouds or haze during the fire season, such as tropical and boreal forests, have low pFRP due to our assumption that the cloud-gap corrections in these inventories successfully capture the fires obscured by clouds/haze.

4.2 Comparison of global fire emissions inventories: speciation and emissions factors

We find inconsistencies in the speciation of the overall emissions budget for CO_2, CO, CH_4, OC, BC, and $PM_{2.5}$ across the five global fire emissions inventories. For example, QFEDv2.5r1 and FEERv1.0-G1.2 estimate ~2-3 times as much OC, BC, and $PM_{2.5}$ emissions than the other inventories, with QFEDv2.5r1 higher than FEERv1.0-G1.2 (Table 2). Mean annual OC + BC emissions, from 2003-2016, among inventories differ by 5-126% in coefficient

of variation (CV; Figure 6). In regions with a high CV, such as temperate North America (102%) and the Middle East (126%), QFEDv2.5r1 OC+BC emissions dominate the emissions from other inventories. These discrepancies shed light on the impact of the different algorithms that convert burned area or fire energy into aerosol emissions. For example, QFED and FEER apply top-down constraints on aerosol emissions to match smoke AOD, while such adjustments are absent in GFED, FINN, and GFAS. FEER uses smoke AOD to directly calculate TPM, which is then broken down into aerosol species, while QFED enhances aerosol emissions with a constant global scaling factor for each LULC (Darmenov and da Silva, 2013; Ichoku and Ellison, 2014). Using MODIS/Aqua AOD, however, Darmenov and da Silva (2013) find significant variation in these scaling factors across each LULC – e.g., from 2-3 in tropical forest, 3-5 in extratropical forests, and 1-3 in grasslands and savanna.

To better understand the discrepancies across inventory emissions, we examine the emissions factors used in GFEDv4s and in earlier versions of FINN, GFAS, and QFED: FINNv1.0, GFASv1.0, and QFEDv2.4. (Emissions factors for the current versions of these three inventories are not publicly available, and we assume that they do not deviate significantly than those in previous versions.) First, we assess the impact of LULC classification on emissions factors by deriving a globally averaged emissions factor for each emitted species in each inventory, weighted by the total dry matter emissions for each LULC. To isolate the differences in LULC classification among inventories, we use the GFEDv4s dry matter emissions partitioned by LULC for the weighting. Since FINN subdivides the GFED4s savanna, grasslands, and shrublands LULC into two smaller LULC, we derive weights for these LULC using FINNv1.5 emissions. We find that the coefficients of variation in emission factors across the four inventories are relatively small for CO_2, CO, OC, and BC (1.75-6.67%), compared to those for CH_4 and $PM_{2.5}$ (20.3-26.7%; Table 3). GFEDv4s and GFAS, which consider peatlands as a separate LULC, have about 60% higher weighted mean emissions factors for CH_4 than FINN and QFED. This discrepancy arises because the peat emissions factor (20.8 g CH_4 kg^{-1} dry matter) is 150-1290% higher than the CH_4 emissions factors for other LULC (Table 3, Table S1), and only GFEDv4s and GFAS consider peatlands separately. The high CH_4, as well as CO, emissions factors for peat fires can be attributed to incomplete combustion from smoldering fires, which are common in boreal and tropical peatlands (Kasischke and Bruhwiler, 2002; Stockwell et al., 2016). Additionally, the $PM_{2.5}$ emissions factors used in FINN for savanna, grassland, and shrubland (8.3-15.4 g $PM_{2.5}$ kg^{-1} dry matter) are 16-214% higher than those used in GFEDv4s, GFAS, QFED (4.9-7.17 g $PM_{2.5}$ kg^{-1} dry matter) for the broader savanna, grassland, and shrubland LULC, which may explain the high $PM_{2.5}$ weighted mean emissions factor for FINN (Table S1).

4.3 Modeling monthly smoke $PM_{2.5}$ from Indonesia fires

We use monthly GEOS-Chem adjoint sensitivities, from 2005-2009, with the five global fire emissions inventories to model smoke $PM_{2.5}$ in Singapore, Malaysia, and Indonesia from 2003-2016, focusing on the impact of the Indonesian fires upwind (Figure 7-8, S7-8). Modeled monthly mean smoke $PM_{2.5}$ is moderately to strongly correlated with observations (r = 0.64 to 0.84, $p < 0.01$), with GFASv1.2 smoke $PM_{2.5}$ most closely matching the temporal variability of observed $PM_{2.5}$ enhancement from smoke (Figure 8a). We find similarly strong correlations for population-weighted smoke PM_{10} in Malaysia (r = 0.54 to 0.88, $p < 0.01$) and satellite AOD in Indonesia (r = 0.63 to 0.93, $p < 0.01$; Figures S7-S8). While the correlation of modeled and observed smoke $PM_{2.5}$ in Singapore is consistent across inventories, the magnitude of modeled smoke $PM_{2.5}$ can differ by more than 20 μg m^{-3} for the Jul-Oct average during extreme smoke

episodes, such as in 2006 and 2015 (Figure 8b). For example, the models yield mean Jul-Oct smoke $PM_{2.5}$ concentrations in 2006 that differ from observed smoke by -64% to +70%. For the 2006, 2009 and 2015 high fire years, modeled Jul-Oct smoke $PM_{2.5}$ using GFASv1.2 yields the smallest mean absolute error relative to the observations (16%), compared to such errors from the other four inventories (39-66%).

4.3.1. 2006 and 2015 severe haze events

Using GFASv1.0 and the GEOS-Chem adjoint, Koplitz et al. (2016) estimate over 150% higher premature mortality in Equatorial Asia in 2015 (100,300 excess deaths) than in 2006 (37,600 excess deaths). This suggests higher smoke exposure and fire activity, as well as drier conditions, in 2015 compared to 2006. We first compare relative changes in modeled Jul-Oct mean smoke exposure in Singapore between the 2006 and 2015 fire seasons. In addition, the strong negative exponential relationship between dry season rainfall and metrics of fire activity (e.g., active fire count, burned area) in Indonesia is well-established (Fernandes et al., 2017; van der Werf et al., 2017). However, Cusworth et al. (2018) suggest that thick haze may obscure fires from satellite detection. To determine whether fire activity in Equatorial Asia is under-detected in 2015 due to haze, we first model the linear relationship between rainfall and fire activity, as well as with satellite AOD, in the log-log space for the 2003-2016 period. We use Jul-Oct rainfall rates from CHIRPS and MxD08_M3 AOD. As measures of seasonal mean fire activity, we use the MxD14A1 active fire mask, MxD14A1 FRP, and MCD64A1 burned area, averaged over the Indonesian provinces of Sumatra and Kalimantan, where most fires are concentrated. We then predict 2015 fires in the context of the log-log linear regression of rainfall and fires, modeled excluding 2015 observations. If fires are under-detected due to haze in 2015, then active fire counts, FRP, and burned area should deviate negatively from the modeled log-log rainfall-fire relationships, compared to AOD, which should not deviate significantly.

Several phenomena indicate a more severe haze episode in 2015 than in 2006. The Niño 3.4 index, which is a proxy for ENSO and based on anomalies in tropical Pacific sea surface temperatures, suggests a stronger El Niño in 2015 than in 2006 (Koplitz et al., 2016). In addition, lower rainfall rates (-29%) and higher AOD (+31-34%) over Sumatra and Kalimantan in 2015 suggest drier and hazier conditions over these fire-prone regions, relative to 2006. In contrast, minimal increases in active fire count (+6%) and FRP (+10%) in 2015 relative to the long-term MODIS record, and even decreases in burned area (-35%) suggest that increased haziness in 2015 may have obscured many fires, making detection by satellites challenging. During the Indonesia fire season (Jul-Oct), satellite-observed smoke AOD and indicators of fire activity strongly correlate with rainfall in log-log space over 2003-2016 when 2015 is excluded (r = -0.87 to -0.98, $p < 0.01$; Figure 9). Given these relationships with rainfall, the 2015 fire activity appears severely underestimated, with active fire 60% less than expected, burned area 93% less, and FRP 62% less. In contrast, AOD in 2015 does not deviate significantly (-12%) from the modeled log-log relationship with rainfall.

The observed AOD and FRP in 2015 are within the 95% prediction interval for these variables, but burned area and active fire counts are outside this interval. We now examine how these potential underestimates in 2015 fire activity may have affected the fire emissions inventories. We find that GFEDv4s, which includes a small fires boost, and FINNv1.5, which uses active fires to estimate burned area, less severely underestimate (63-76%) burned area in 2015 than the MODIS burned area product (Figure S4). Inventories that make cloud-gap adjustments for obscured fires are better able to discern the more severe haze event in 2015 and match the observed enhancement in smoke $PM_{2.5}$ in Singapore of +183%: GFASv1.2 shows a

+155% increase in smoke $PM_{2.5}$ relative to 2006, and QFEDv2.5r1 and FEERv1.0-G1.2 yield increases of +96-137%. In contrast, GFEDv4s and FINNv1.5 do not capture the enhanced smoke $PM_{2.5}$ in Singapore in 2015 (Figure 8b). Overall, GFASv1.2 most accurately captures both the magnitude and temporal variability of observed smoke $PM_{2.5}$, while FINNv1.5 consistently underestimates smoke $PM_{2.5}$ in high fire years and most poorly captures the temporal variability of observed smoke $PM_{2.5}$.

5. Discussion and Conclusions

5.1 Relative fire confidence metrics: spatial patterns

The goal of this study has been to quantify and interpret differences across five bottom-up and top-down global fire emission inventories. While it is difficult to directly compare bottom-up and top-down inventories, end-users may use the relative confidence indicated by the BA-score, AFA-score, and FRP-score (pFRP) to select a "best" inventory if limited by computing resources or assess the five relative fire confidence metrics individually. We first find that two fire landscapes – large and cohesive versus small and fragmented – account for broad differences in the bottom-up fire emissions inventories, GFED and FINN. GFED, which relies primarily on observed burned area, better captures emissions from large, cohesive fires, while FINN, which depends on observed active fires, better diagnoses emissions from small, fragmented fires. Second, the presence of thick cloud/haze during peak fire activity enhances the difficulty in fire detection in equatorial regions, boreal regions, and eastern China. Third, fires located in mountainous regions are also challenging to detect, especially by moderate-resolution sensors, such as MODIS (500 m or 1 km) or VIIRS (375 m or 750 m). For top-down fire emissions inventories (e.g., GFAS, QFED, and FEER), we calculate a pFRP score, which indicates potential underestimates in FRP under clear-sky conditions. We find high pFRP scores suggest that areas dominated by fast-spreading, large fires or short-lived, small fires under clear-sky conditions are not captured well by MODIS due to limited overpasses or moderate spatial resolution.

5.2 Regional application: validation of modeled smoke $PM_{2.5}$ across Equatorial Asia from Indonesia fires

Here we discuss the application of the relative fire confidence metrics for Indonesia fires. (Additional examples for the contiguous United States and northwestern India are discussed in Supplementary Section S6.) We can first deduce that fire-prone regions in Indonesia generally follow the small, fragmented fire landscape pattern (metrics 1, 3, and 5) and that high cloud cover and/or haze (metric 2) may impede observation during the fire season. While metric 4 shows rough terrain in parts of Indonesia (e.g., western Sumatra, Java, and northern Kalimantan), most fires occur on flat terrain. However, smoldering subsurface peat fires even on flat land may also be difficult to detect.

First, we find that thick haze in very high fire years, such as 2015, likely leads to lower-than-expected fire activity derived from satellite observations. The AFA-score suggests high relative confidence for FINN, in contrast to the low relative confidence by BA-score for GFED; pFRP shows low potential FRP enhancement over Indonesia, primarily because of the presence of thick clouds or haze. Our results suggest that the 93% burned area underestimate in Indonesia arises primarily due to thick haze, an effect greater than the effect of such haze on active fire count (-60%) or FRP (-62%). For Singapore, as well as for Malaysia and Indonesia, we find that top-down inventories yield modeled smoke $PM_{2.5}$ concentrations that are more consistent with

observed $PM_{2.5}$ than bottom-up inventories, with r = 0.78-0.84 for top-down versus r = 0.64-0.73 for bottom-up inventories. This result is likely due to the cloud-gap adjustments in the top-down inventories.

Second, only GFAS and GFED consider peatlands as a separate LULC, while in other inventories, peatlands may be classified as savanna, tropical forest, or cropland. These discrepancies have implications for emissions since the carbon-rich peatlands are associated with high OC emissions, and in particular, with OC to BC emissions ratios of about 150 compared to just 3-39 in other LULC types. Indeed, GFEDv4s and GFASv1.2 show 78-380% higher Jul-Oct OC to BC ratios over Sumatra and Kalimantan during 2003-2016 than the other three inventories. While the moderate to strong correlation of observed and modeled smoke $PM_{2.5}$ is consistent across inventories, the magnitude of mean Jul-Oct smoke $PM_{2.5}$ in the high fire years of 2006 and 2015 varies significantly, with GFEDv4s and GFASv1.2 better capturing the magnitude of observed smoke $PM_{2.5}$ and yielding higher smoke $PM_{2.5}$ than the other inventories. In summary, GFASv1.2, which adjusts for cloud gaps in satellite observations of fires and considers peatlands as a separate LULC class, performs best in terms of modeling smoke $PM_{2.5}$ that is consistent with observations in both temporal variability and magnitude.

5.3 Uncertainties in global fire emissions inventories

The uncertainties in global fire emissions inventories influence estimates of emissions budgets, the spatio-temporal variability of fires, and fire trends, with different inventories leading to different conclusions (Supplementary Section S7). Here we discuss the main sources of uncertainty in inventories: small fires, cloud gap adjustments, aerosol emissions enhancements, and emissions factors and LULC classification. Sole reliance on burned area from MCD64A1 may capture large, contiguous fires well but not the spatial allocation of small fires in a fragmented burn landscape. This is demonstrated by the moderate spatial correlation (r = 0.36, p < 0.01) between the BA-AFA discrepancy (metric 1) and burn size/fragmentation (metric 3). Additional VIIRS FRP detected outside the MODIS active fire extent (metric 5) also implies low confidence in areas dominated by small fires. As an example of low confidence in small fires, we find that many grid cells in GFEDv4s would not have any emissions without the small fires boost. Approximately one-fourth of grid cells with nonzero GFEDv4s fire emissions from 2003-2016 persistently show 100% spatial coverage by small fires, and the small fire boost alone contributes all emissions in 57% of GFEDv4s grid cells, on average. Zhang et al. (2018) recommended that grid cells with only small fire contribution, or no MCD64A1 burned area input, be treated with caution. For example, these authors found that GFEDv4s significantly overestimates dry matter fuel consumption and emissions for areas with infrequent but small fires in eastern China during summer months. Under such conditions, when no area burned is detected, the scaling parameters applied to the total active fire count are not specific to individual grid cells and instead are averaged across regions, seasons, and land cover types (van der Werf et al., 2017). On the other hand, because MODIS retrieves thermal anomalies only during satellite overpass times, use of MxD14A1 or MCD14ML active fires in the bottom-up inventories, as well as FRP in the top-down inventories, may lead to underestimates of burned area and fire energy from large, contiguous fires. In addition, the FINN emissions inventory may overrepresent small fire emissions due to the assumption that at least 75% of the nominal pixel area is burned (Wiedinmyer et al., 2011). The active fire product also has coarser resolution and a lower detection threshold compared to the burned area product. Using FRP may address this overestimate since small fires are cooler. On the other hand, the dependence of the top-down inventories on GFED to convert FRP to dry matter burned may lead to underestimates of small

fire emissions, as seen in the case of agricultural fire emissions in northwestern India (Cusworth et al., 2018).

The cloud/haze fraction (metric 2) indicates that regions with persistent cloud cover or thick haze during the fire season, such as boreal and tropical regions, degrade the quality of satellite observations of fire activity. By adjusting for cloud gaps and scaling with observed AOD, the top-down inventories – GFASv1.2, QFEDv2.5r1 and FEERv1.0-G1.2 – may be better able to match observations than the bottom-up inventories in these regions (Koplitz et al., 2018). However, the scaling factor of 3.4 recommended by Kaiser et al. (2012) for GFAS aerosol emissions, as well as the simple global QFED scaling by LULC, may bias regional smoke exposure estimates (e.g., Koplitz et al., 2016) due to spatial variations in AOD scaling (Darmenov and da Silva, 2013; Ichoku and Ellison, 2014). We thus recommend comparison of aerosol emissions from QFEDv2.5r1 to FEERv1.0-G1.2, which directly estimates TPM using smoke AOD by region. Further, QFED calibrates the coefficient β relating FRP to dry matter globally, while GFAS uses LULC-specific β coefficients, which vary from 0.13 to 5.87 kg dry matter MJ^{-1} FRP (Kaiser et al., 2012). We also show that certain species, such as CH_4, are significantly affected by LULC classification within the inventories, and in particular, by the treatment of peatland emissions. In our case study of Indonesian fires, GFEDv4s and GFASv1.2, both of which account for peatlands, yield much higher smoke $PM_{2.5}$ more in line with observations than the other three inventories. However, coarse-resolution LULC maps (0.5°-1°), which are used in GFASv1.2 and FEERv1.0-G1.2, may also bias emissions due to differences in fuel loadings in regions with more heterogenous LULC, such as in Southeast Asia (Figure S10b).

5.4 Future directions and recommendations

Integration of both burned area and active fire products into fire emission inventories may reduce underestimation of fires in small and fragmented or large and contiguous fire regions, respectively. Similar to the use of active fires for the small fire boost in GFEDv4s, incorporation of burned area in FINN could improve the emissions from large fires. For the top-down inventories of GFAS, QFED, and FEER, use of burned area as a secondary input satellite fire dataset would yield emissions more closely based on observations rather than on assumptions of fire persistence across cloud gaps. Standardization of emissions factors, in particular in the partitioning of LULC could help reduce inconsistencies between inventories. Further, access to the high-resolution, surface reflectance datasets Landsat (30 m) and Sentinel (10 m) in the GEE data catalog makes feasible both ground truth validation and improvement of burned area estimates and LULC classification (Casu et al., 2017).

For end-users, we recommend use of multiple bottom-up and top-down inventories, if possible. Further, end-users should be aware that outdated emissions estimates can persist in models, leading to biases and errors in model results (Supplementary Section S8). We present here an online tool, "Fire Inventories: Regional Evaluation, Comparison, and Metrics" (FIRECAM; https://globalfires.earthengine.app/view/firecam), that allows users to compare regional monthly and yearly emissions, from 2003-2016, from the five global inventories for six species (CO, CO_2, CH_4, OC, BC, and $PM_{2.5}$) and to interpret the regional differences between fire emissions by using the five relative fire confidence metrics (Figure S11, Supplementary Section S5). We identify three key factors that should influence the end-user's inventory selection and can also significantly affect the results of modeling studies: input satellite fire dataset, statistical adjustments, and LULC classification and emissions factors. For example, in our case study on Indonesian fires, we find the cloud-gap adjustment and representation of peatland emissions are two important factors that distinguish different inventories in the regional

validation of smoke $PM_{2.5}$; both factors are included in the GFAS inventory. FIRECAM allows users to rapidly assess such differences in regional fire emissions.

Acknowledgements

T. Liu is funded by a NSF Graduate Research Fellowship (NSF grant DGE1745303). We acknowledge the Singapore National Environment Agency (NEA) and Malaysian Department of Environment (DOE) for maintaining a network of stations that provide continuous air quality measurements across Singapore and Malaysia.

References

Akagi, S.K., Yokelson, R.J., Wiedinmyer, C., Alvarado, M.J., Reid, J.S., Karl, T., Crounse, J.D., Wennberg, P.O., 2011. Emission factors for open and domestic biomass burning for use in atmospheric models. Atmos. Chem. Phys. 11, 4039–4072. https://doi.org/10.5194/acp-11-4039-2011

Andela, N., Morton, D.C., Giglio, L., Paugam, R., Chen, Y., Hantson, S., van der Werf, G.R., Randerson, J.T., 2018. The Global Fire Atlas of individual fire size, duration, speed, and direction. Earth Syst. Sci. Data Discuss. 1–28. https://doi.org/10.5194/essd-2018-89

Andreae, M.O., Merlet, P., 2001. Emissions of trace gases and aerosols from biomass burning. Global Biogeochem. Cycles 15, 955–966. https://doi.org/10.1029/2000GB001382

Casu, F., Manunta, M., Agram, P.S., Crippen, R.E., 2017. Big Remotely Sensed Data: tools, applications and experiences. Remote Sens. Environ. 202, 1–2. https://doi.org/10.1016/j.rse.2017.09.013

Chen, Y., Morton, D.C., Andela, N., van der Werf, G.R., Giglio, L., Randerson, J.T., 2017. A pan-tropical cascade of fire driven by El Niño/Southern Oscillation. Nat. Clim. Chang. 7, 906–911. https://doi.org/10.1038/s41558-017-0014-8

Crippa, P., Castruccio, S., Archer-Nicholls, S., Lebron, G.B., Kuwata, M., Thota, A., Sumin, S., Butt, E., Wiedinmyer, C., Spracklen, D. V., 2016. Population exposure to hazardous air quality due to the 2015 fires in Equatorial Asia. Sci. Rep. 6, 1–9. https://doi.org/10.1038/srep37074

Cusworth, D.H., Mickley, L.J., Sulprizio, M.P., Liu, T., Marlier, M.E., DeFries, R.S., Guttikunda, S.K., Gupta, P., 2018. Quantifying the influence of agricultural fires in northwest India on urban air pollution in Delhi, India. Environ. Res. Lett. 13, 044018. https://doi.org/10.1088/1748-9326/aab303

Darmenov, A.S., da Silva, A., 2013. The Quick Fire Emissions Dataset (QFED) - Documentation of versions 2.1, 2.2, and 2.4, NASA Technical Report Series on Global Modeling and Data Assimilation, Volume 32.

Dennis, R.A., Mayer, J., Applegate, G., Chokkalingam, U., Colfer, C.J.P., Kurniawan, I., Lachowski, H., Maus, P., Permana, R.P., Ruchiat, Y., Stolle, F., Suyanto, Tomich, T.P., 2005. Fire, people and pixels: Linking social science and remote sensing to understand underlying causes and impacts of fires in Indonesia. Hum. Ecol. 33, 465–504. https://doi.org/10.1007/s10745-005-5156-z

Fernandes, K., Verchot, L., Baethgen, W., Gutierrez-Velez, V., Pinedo-Vasquez, M., Martius, C., 2017. Heightened fire probability in Indonesia in non-drought conditions: the effect of increasing temperatures. Environ. Res. Lett. 12, 054002. https://doi.org/10.1088/1748-9326/aa6884

Funk, C., Peterson, P., Landsfeld, M., Pedreros, D., Verdin, J., Shukla, S., Husak, G., Rowland, J., Harrison, L., Hoell, A., Michaelsen, J., 2015. The climate hazards infrared precipitation with stations - A new environmental record for monitoring extremes. Sci. Data 2, 1–21. https://doi.org/10.1038/sdata.2015.66

Giglio, L., 2007. Characterization of the tropical diurnal fire cycle using VIRS and MODIS observations. Remote Sens. Environ. 108, 407–421. https://doi.org/10.1016/j.rse.2006.11.018

Giglio, L., Boschetti, L., Roy, D.P., Humber, M.L., Justice, C.O., 2018. The Collection 6 MODIS burned area mapping algorithm and product. Remote Sens. Environ. 217, 72–85. https://doi.org/10.1016/j.rse.2018.08.005

Giglio, L., Csiszar, I., Justice, C.O., 2006. Global distribution and seasonality of active fires as observed with the Terra and Aqua Moderate Resolution Imaging Spectroradiometer (MODIS) sensors. J. Geophys. Res. Biogeosciences 111, 1–12. https://doi.org/10.1029/2005JG000142

Giglio, L., Descloitres, J., Justice, C.O., Kaufman, Y.J., 2003. An enhanced contextual fire detection algorithm for MODIS. Remote Sens. Environ. 87, 273–282. https://doi.org/10.1016/S0034-4257(03)00184-6

Giglio, L., Loboda, T., Roy, D.P., Quayle, B., Justice, C.O., 2009. An active-fire based burned area mapping algorithm for the MODIS sensor. Remote Sens. Environ. 113, 408–420. https://doi.org/10.1016/j.rse.2008.10.006

Giglio, L., Schroeder, W., Justice, C.O., 2016. The collection 6 MODIS active fire detection algorithm and fire products. Remote Sens. Environ. 178, 31–41. https://doi.org/10.1016/j.rse.2016.02.054

Gorelick, N., Hancher, M., Dixon, M., Ilyushchenko, S., Thau, D., Moore, R., 2017. Google Earth Engine: Planetary-scale geospatial analysis for everyone. Remote Sens. Environ. 202, 18–27. https://doi.org/10.1016/j.rse.2017.06.031

Gras, J.L., Jensen, J.B., 1999. Some Optical Properties of Smoke Aerosol in Indonesia. Geophys. Res. Lett. 26, 1393–1396.

Hall, J. V., Loboda, T. V., Giglio, L., McCarty, G.W., 2016. A MODIS-based burned area assessment for Russian croplands: Mapping requirements and challenges. Remote Sens. Environ. 184, 506–521. https://doi.org/10.1016/j.rse.2016.07.022

Hayasaka, H., Noguchi, I., Putra, E.I., Yulianti, N., Vadrevu, K., 2014. Peat-fire-related air pollution in Central Kalimantan, Indonesia. Environ. Pollut. 195, 257–266. https://doi.org/10.1016/j.envpol.2014.06.031

Heymann, J., Reuter, M., Buchwitz, M., Schneising, O., Bovensmann, H., Burrows, J.P., Massart, S., Kaiser, J.W., Crisp, D., 2017. CO2 emission of Indonesian fires in 2015 estimated from satellite-derived atmospheric CO2 concentrations. Geophys. Res. Lett. 44, 1537–1544. https://doi.org/10.1002/2016GL072042

Hoelzemann, J.J., Schultz, M.G., Brasseur, G.P., Granier, C., Simon, M., 2004. Global Wildland Fire Emission Model (GWEM): Evaluating the use of global area burnt satellite data. J. Geophys. Res. D Atmos. 109. https://doi.org/10.1029/2003JD003666

Ichoku, C., Ellison, L., 2014. Global top-down smoke-aerosol emissions estimation using satellite fire radiative power measurements. Atmos. Chem. Phys. 14, 6643–6667. https://doi.org/10.5194/acp-14-6643-2014

Kaiser, J.W., Heil, A., Andreae, M.O., Benedetti, A., Chubarova, N., Jones, L., Morcrette, J.J., Razinger, M., Schultz, M.G., Suttie, M., van der Werf, G.R., 2012. Biomass burning emissions estimated with a global fire assimilation system based on observed fire radiative power. Biogeosciences 9, 527–554. https://doi.org/10.5194/bg-9-527-2012

Kasischke, E.S., Bruhwiler, L.P., 2002. Emissions of carbon dioxide, carbon monoxide, and methane from boreal forest fires in 1998. J. Geophys. Res. 108, 8146. https://doi.org/10.1029/2001JD000461

Kim, P.S., Jacob, D.J., Mickley, L.J., Koplitz, S.N., Marlier, M.E., DeFries, R.S., Myers, S.S., Chew, B.N., Mao, Y.H., 2015. Sensitivity of population smoke exposure to fire locations in Equatorial Asia. Atmos. Environ. 102, 11–17. https://doi.org/10.1016/j.atmosenv.2014.09.045

Koplitz, S.N., Mickley, L.J., Marlier, M.E., Buonocore, J.J., Kim, P.S., Liu, T., Sulprizio, M.P., DeFries, R.S., Jacob, D.J., Schwartz, J., Pongsiri, M., Myers, S.S., 2016. Public health impacts of the severe haze in Equatorial Asia in September–October 2015: demonstration of a new framework for informing fire management strategies to reduce downwind smoke exposure. Environ. Res. Lett. 11, 094023. https://doi.org/10.1088/1748-9326/11/9/094023

Koplitz, S.N., Nolte, C.G., Pouliot, G.A., Vukovich, J.M., Beidler, J., 2018. Influence of uncertainties in burned area estimates on modeled wildland fire PM2.5 and ozone pollution in the contiguous U.S. Atmos. Environ. 191, 328–339. https://doi.org/10.1016/j.atmosenv.2018.08.020

Maasakkers, J.D., Jacob, D.J., Sulprizio, M.P., Turner, A.J., Weitz, M., Wirth, T., Hight, C., DeFigueiredo, M., Desai, M., Schmeltz, R., Hockstad, L., Bloom, A.A., Bowman, K.W., Jeong, S., Fischer, M.L., 2016. Gridded National Inventory of U.S. Methane Emissions. Environ. Sci. Technol. 50, 13123–13133. https://doi.org/10.1021/acs.est.6b02878

Marlier, M.E., DeFries, R.S., Kim, P.S., Koplitz, S.N., Jacob, D.J., Mickley, L.J., Myers, S.S., 2015. Fire emissions and regional air quality impacts from fires in oil palm, timber, and logging concessions in Indonesia. Environ. Res. Lett. 10, 085005. https://doi.org/10.1088/1748-9326/10/8/085005

Marlier, M.E., Liu, T., Yu, K., Buonocore, J.J., Koplitz, S.N., DeFries, R.S., Mickley, L.J., Jacob, D.J., Schwartz, J., Wardhana, B.S., Myers, S.S., n.d. Fires, Smoke Exposure, and Public Health: An Integrative Framework to Maximize Health Benefits from Peatland Restoration.

Prentice, I.C., Kelley, D.I., Foster, P.N., Friedlingstein, P., Harrison, S.P., Bartlein, P.J., 2011. Modeling fire and the terrestrial carbon balance. Global Biogeochem. Cycles 25, GB3005. https://doi.org/10.1029/2010GB003906

Rein, G., Cleaver, N., Ashton, C., Pironi, P., Torero, J.L., 2008. The severity of smouldering peat fires and damage to the forest soil. Catena 74, 304–309.

https://doi.org/10.1016/j.catena.2008.05.008

Rogers, B.M., Soja, A.J., Goulden, M.L., Randerson, J.T., 2015. Influence of tree species on continental differences in boreal fires and climate feedbacks. Nat. Geosci. 8, 228–234. https://doi.org/10.1038/ngeo2352

Schroeder, W., Giglio, L., 2017. Visible Infrared Imaging Radiometer Suite (VIIRS) 375 m & 750 m Active Fire Detection Data Sets Based on NASA VIIRS Land Science Investigator Processing System (SIPS) Reprocessed Data - Version 1.

Shi, Y., Matsunaga, T., Saito, M., Yamaguchi, Y., Chen, X., 2015. Comparison of global inventories of CO2 emissions from biomass burning during 2002-2011 derived from multiple satellite products. Environ. Pollut. 206, 479–487. https://doi.org/10.1016/j.envpol.2015.08.009

Stockwell, C.E., Jayarathne, T., Cochrane, M.A., Ryan, K.C., Putra, E.I., Saharjo, B.H., Nurhayati, A.D., Albar, I., Blake, D.R., Simpson, I.J., Stone, E.A., Yokelson, R.J., 2016. Field measurements of trace gases and aerosols emitted by peat fires in Central Kalimantan, Indonesia, during the 2015 El Niño. Atmos. Chem. Phys. 16, 11711–11732. https://doi.org/10.5194/acp-16-11711-2016

Tosca, M.G., Randerson, J.T., Zender, C.S., 2013. Global impact of smoke aerosols from landscape fires on climate and the Hadley circulation. Atmos. Chem. Phys. 13, 5227–5241. https://doi.org/10.5194/acp-13-5227-2013

van der Werf, G.R., Dempewolf, J., Trigg, S.N., Randerson, J.T., Kasibhatla, P.S., Giglio, L., Murdiyarso, D., Peters, W., Morton, D.C., Collatz, G.J., Dolman, A.J., DeFries, R.S., 2008. Climate regulation of fire emissions and deforestation in equatorial Asia. Proc. Natl. Acad. Sci. 105, 20350–20355. https://doi.org/10.1073/pnas.0803375105

van der Werf, G.R., Randerson, J.T., Giglio, L., Collatz, G.J., Mu, M., Kasibhatla, P.S., Morton, D.C., Defries, R.S., Jin, Y., Van Leeuwen, T.T., 2010. Global fire emissions and the contribution of deforestation, savanna, forest, agricultural, and peat fires (1997-2009). Atmos. Chem. Phys. 10, 11707–11735. https://doi.org/10.5194/acp-10-11707-2010

van der Werf, G.R., Randerson, J.T., Giglio, L., van Leeuwen, T.T., Chen, Y., Rogers, B.M., Mu, M., van Marle, M.J.E., Morton, D.C., Collatz, G.J., Yokelson, R.J., Kasibhatla, P.S., 2017. Global fire emissions estimates during 1997–2016. Earth Syst. Sci. Data 9, 697–720. https://doi.org/10.5194/essd-9-697-2017

Wiedinmyer, C., Akagi, S.K., Yokelson, R.J., Emmons, L.K., Orlando, J.J., Soja, A.J., 2011. The Fire INventory from NCAR (FINN): a high resolution global model to estimate the emissions from open burning. Geosci. Model Dev. 4, 625–641. https://doi.org/10.5194/gmd-4-625-2011

Wilson, A.M., Jetz, W., 2016. Remotely Sensed High-Resolution Global Cloud Dynamics for Predicting Ecosystem and Biodiversity Distributions. PLoS Biol. 14, 1–20. https://doi.org/10.1371/journal.pbio.1002415

Wooster, M.J., Roberts, G., Perry, G.L.W., Kaufman, Y.J., 2005. Retrieval of biomass combustion rates and totals from fire radiative power observations: FRP derivation and calibration relationships between biomass consumption and fire radiative energy release. J. Geophys. Res. Atmos. 110, 1–24. https://doi.org/10.1029/2005JD006318

Xiang, H., Liu, J., Cao, C., Xu, M., 2013. Algorithms for Moderate Resolution Imaging

Spectroradiometer cloud-free image compositing. J. Appl. Remote Sens. 7, 073486. https://doi.org/10.1117/1.JRS.7.073486

Yi, Y., Kimball, J.S., Reichle, R.H., 2014. Spring hydrology determines summer net carbon uptake in northern ecosystems. Environ. Res. Lett. 9, 064003. https://doi.org/10.1088/1748-9326/9/6/064003

Zhang, F., Wang, J., Ichoku, C., Hyer, E.J., Yang, Z., Ge, C., Su, S., Zhang, X., Kondragunta, S., Kaiser, J.W., Wiedinmyer, C., da Silva, A., 2014. Sensitivity of mesoscale modeling of smoke direct radiative effect to the emission inventory: A case study in northern sub-Saharan African region. Environ. Res. Lett. 9, 075002. https://doi.org/10.1088/1748-9326/9/7/075002

Zhang, T., Wooster, M.J., de Jong, M.C., Xu, W., 2018. How Well Does the "Small Fire Boost" Methodology Used within the GFED4.1s Fire Emissions Database Represent the Timing, Location and Magnitude of Agricultural Burning? Remote Sens. 10, 823. https://doi.org/10.3390/rs10060823

Table 1. Comprehensive comparison of the global fire emissions inventories for various methodological details and technical parameters

Inventory	GFEDv4s	FINNv1.5	GFASv1.2	QFEDv2.5r1	FEERv1.0-G1.2
	"Bottom-up"		*"Top-down"*		
Primary satellite fire input	MCD64A1 C5.1 burned area (500 m)	MCD14ML C5 active fire area (1 km)	MOD14/MYD14 C5/C6 FRP (1 km)	MOD14/MYD14 C6 FRP (1 km)	GFASv1.2 FRP (0.1°)
Spatio-temporal resolution	0.25°, monthly (daily fraction)	1 km, daily	0.1°, daily	0.1°, daily (0.25° x 0.375°, NRT)	0.1°, daily
Temporal range	1997- (NRT)	2002-2016	2003- (NRT)	2000- (NRT)	2003- (NRT)
Statistical boosts	Small fires boost	x	Cloud gap adjustment		
Conversion to dry matter (DM) emissions	CASA biogeochemical model (van der Werf *et al*, 2010)	Hoelzemann *et al* (2004)	GFAS FRP-GFEDv3 DM conversion factors by LULC	QFED FRP-GFEDv2 DM global calibration	x
Smoke AOD constraints for aerosol emissions	x	x	Recommend 3.4 global scaling	Additional global scaling constants for OC, BC, $PM_{2.5}$	Directly uses FRP-smoke AOD coefficients to derive TPM emissions
Primary land use/ land cover (LULC)	MCD12Q1 (UMD), annual (500 m)	MCD12Q1 (IGBP), 2005 (500 m)	GFEDv3 dominant fire-prone LULC (0.5°)	IGBP-INPE (1 km)	MODIS IGBP dominant fire-prone LULC, 2004 (1°)
Peatland maps	Olson *et al* (2001)	x	Heil *et al* (2010)	x	x
Partitioning of emissions by LULC	yes	yes	x	yes	x
Emissions factors	Akagi et al. (2011) + updates from M.O. Andreae in 2013	Akagi et al. (2011), Andreae & Merlet (2001)	Andreae & Merlet (2001) + updates from literature	Andreae & Merlet (2001)	Andreae & Merlet (2001) + updates from M.O. Andreae in 2014
Speciation	41 species	27 species	42 species	17 species	30 species
Ancillary products	boosted BA, diurnal cycle, NPP	x	cloud-gap adjusted FRP density, plume top/ smoke injection altitude	cloud-gap adjusted FRP density by LULC	x
References	van der Werf *et al* (2017)	Wiedinmyer *et al* (2011)	Kaiser *et al* (2012)	Darmenov and da Silva (2013)	Ichoku and Ellison (2014)

NRT = near real time; CASA = Carnegie Ames Stanford Approach; UMD = University of Maryland; IGBP = International Biosphere-Geosphere Program; INPE = Instituto Nacional De Pesquisas Espaciais (Brazil's National Space Institute); NPP = Net Primary Production

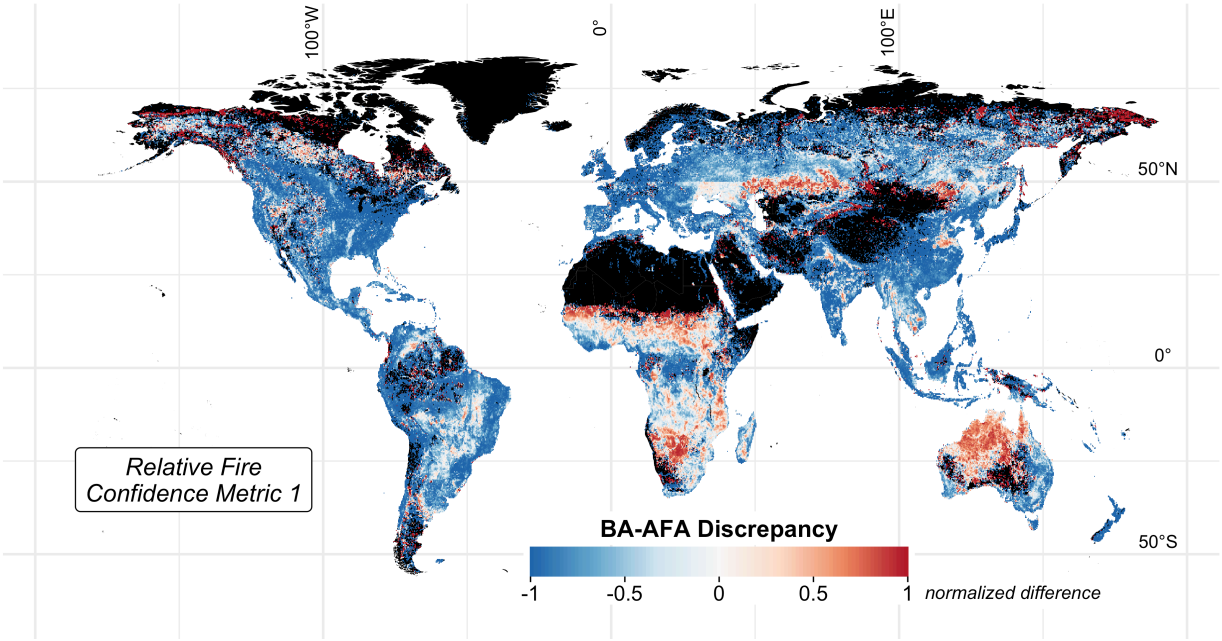

Figure 1. Metric 1 for relative fire confidence score: discrepancy between MCD64A1 burned area (BA) and MxD14A1 active fire area (AFA) based on the normalized difference of BA outside AFA and AFA outside BA. Values are averaged over 2003-2017 and mapped at 0.25° x 0.25° spatial resolution. High values (darker red) indicate relatively more confidence in BA than AFA, and low values (darker blue) the opposite.

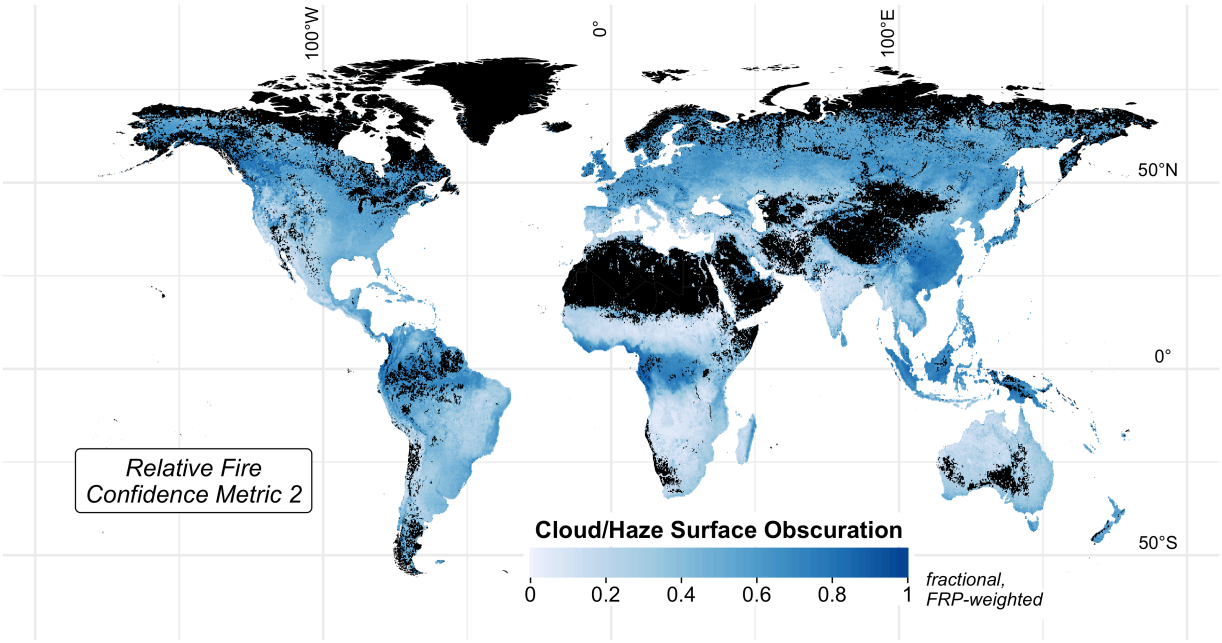

Figure 2. Metric 2 for relative fire confidence score: Cloud/haze fraction based on MxD09GA surface reflectance and weighted by FRP. Values are averaged 2003-2017 and mapped at 0.25° x 0.25° spatial resolution. High FRP-weighted cloud/haze fraction indicates fewer opportunities for satellite observation of the land surface during the fire season.

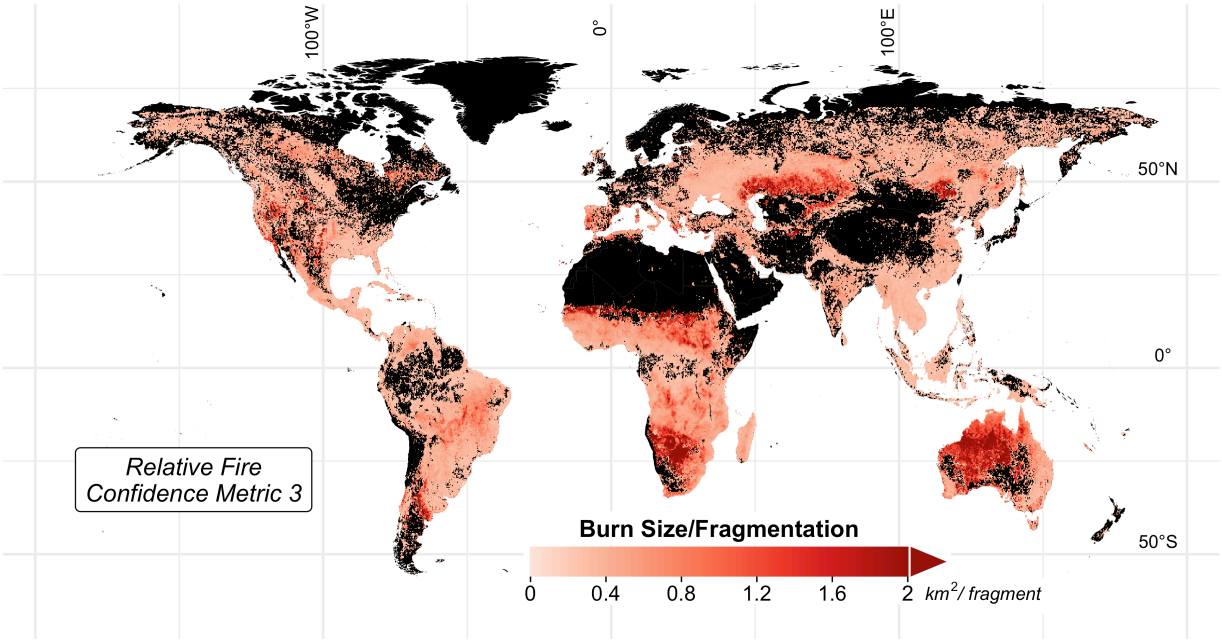

Figure 3. Metric 3 for relative fire confidence score: average burned area (km^2) per "fragment," or contiguous patch of burned area, averaged over 2003-2017 and mapped at 0.25° x 0.25° spatial resolution. High values indicate dominance of large, contiguous fires; low values denote dominance of small, fragmented fires.

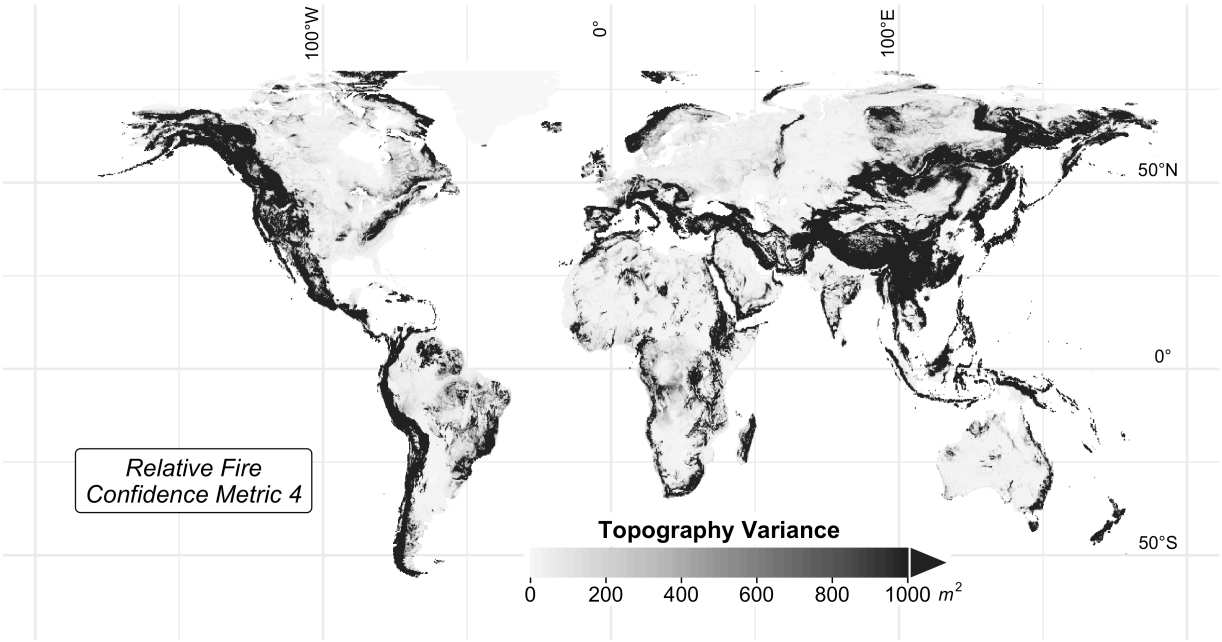

Figure 4. Metric 4 for relative fire confidence score: roughness in topography, expressed as variance in elevation (m^2), averaged over 2003-2017 and mapped at 0.25° x 0.25° spatial resolution. High values in topography variance indicate steep gradients in elevation, or mountainous terrain, whereas low values indicate relatively flat terrain.

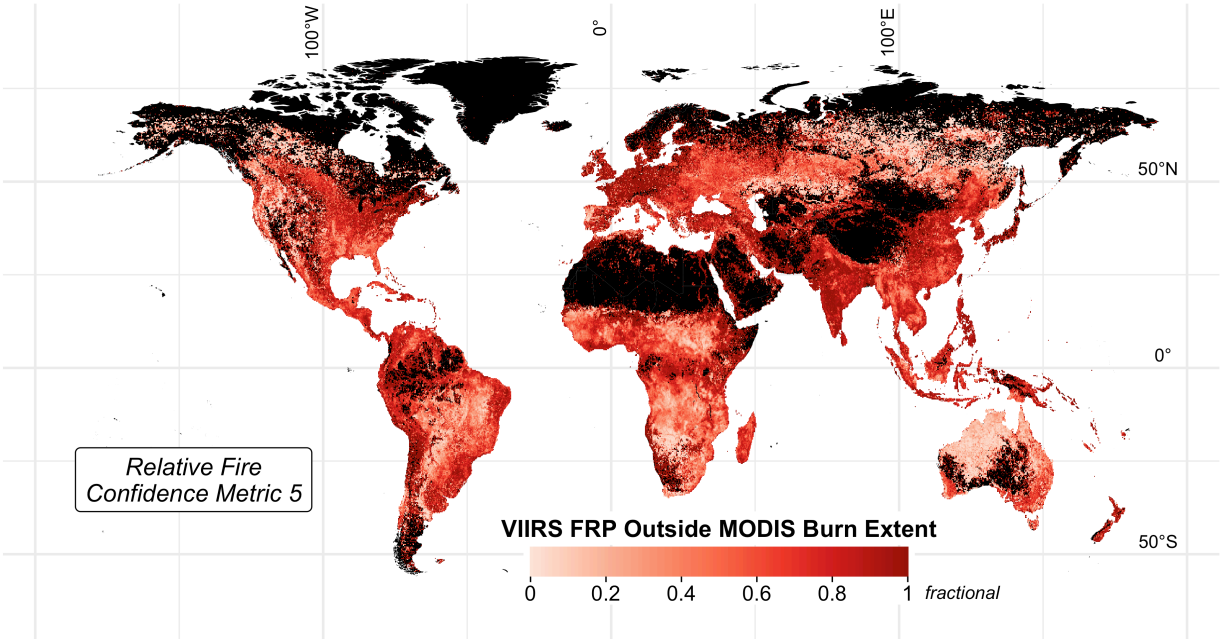

Figure 5. Metric 5 for relative fire confidence score: additional fires detected by VIIRS. Values are the areal fraction of VIIRS FRP occurring outside MODIS burned area and active fire pixel area, averaged over 2003-2017 and mapped at 0.25° x 0.25° spatial resolution. A value of 0 indicates that all VIIRS active fires overlap MODIS active fires, and a value of 1 indicates the presence of VIIRS active fires but no MODIS burned area or active fire observations.

838 **Table 2.** Average annual global CO_2, CO, CH_4, organic carbon (OC), black carbon (BC) and fine
839 particulate matter ($PM_{2.5}$) emissions (Tg yr^{-1}, ±1σ) by inventory, from 2003-2016. The percent
840 difference in emissions relative to GFEDv4s is in brackets. For each species, the inventory with
841 the highest emissions is denoted in red. The coefficient of variation (CV; %) indicates the spread
842 of values, normalized by the mean, across the five inventories.

Species	**Mean Annual Global Emissions (Tg)**					**CV (%)**
	GFEDv4s	*FINNv1.5*	*GFASv1.2*	*QFEDv2.5r1*	*FEERv1.0-G1.2*	
CO_2	6986 (595) --	6292 (1137) [-10%]	7083 (604) [+1%]	7449 (665) [+7%]	13205 (1044) [+89%]	34
CO	336 (39) --	330 (60) [-2%]	366 (43) [+9%]	348 (31) [+4%]	609 (52) [+81%]	30
CH_4	15 (3) --	16 (3) [+7%]	20 (3) [+35%]	15 (1) [+2%]	30 (3) [+103%]	34
OC	16 (2) --	20 (4) [+24%]	19 (2) [+21%]	47 (5) [+199%]	30 (3) [+91%]	49
BC	1.8 (0.2) --	1.9 (0.3) [+7%]	2.1 (0.2) [+15%]	5.3 (0.5) [+196%]	3.9 (0.3) [+119%]	52
$PM_{2.5}$	35 (3) --	35 (6) [+1%]	31 (3) [-11%]	74 (7) [+112%]	51 (4) [+47%]	39

843

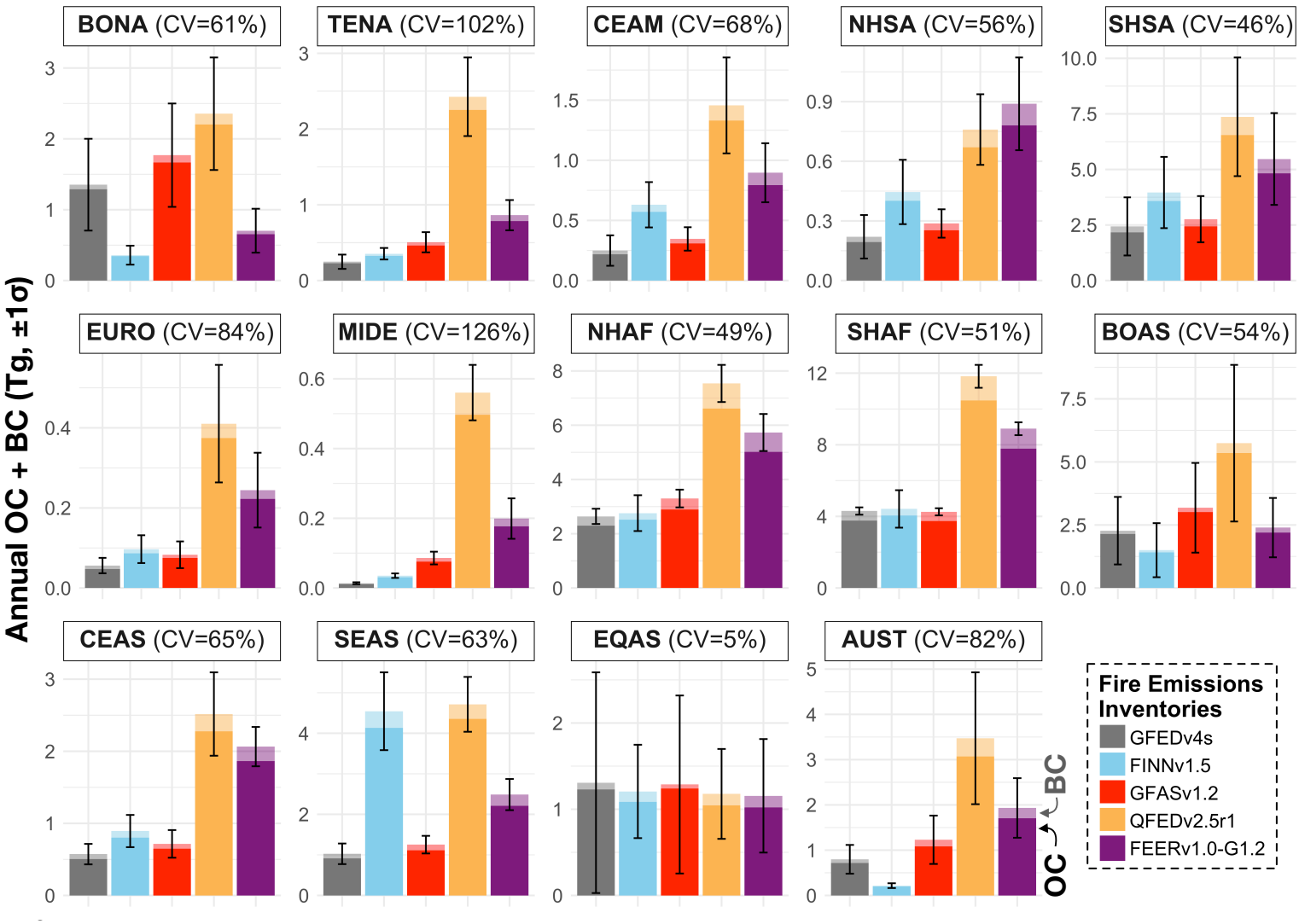

Figure 6. Mean annual OC + BC emissions (Tg yr^{-1}, ±1σ), over 2003-2016, from five global fire emissions inventories (GFEDv4s, FINNv1.5, GFASv1.2, QFEDv2.5r1, and FEERv1.0-G1.2) for the 14 GFEDv4s basis regions (Figure S12; van der Werf et al., 2017). Acronyms for the 14 basis regions are given in Figure S12. The fraction of OC emissions is denoted by darker shades, and that of BC emissions by lighter shades. Vertical bars show one standard deviation of the means over time. The coefficient of variation across inventories (CV, %) is shown for each region.

852 **Table 3.** Average emissions factors (g species kg^{-1} dry matter) for CO_2, CO, CH_4, OC, BC and
853 $PM_{2.5}$, weighted by fractional emissions over GFEDv4s land use/land cover (LULC). The
854 coefficient of variation (CV; %) gives the variation, normalized by the mean, across inventories
855 by species.

Species	**Mean Emissions Factors (g species kg^{-1} dry matter), Weighted by GFEDv4s LULC**				**CV (%)**
	GFEDv4s	*FINNv1.0*	*GFASv1.0*	*QFEDv2.4*	
CO_2	1648	1660	1611	1601	1.75
CO	95	87	91	84	5.45
CH_4	6.67	4.43	7.1	4.2	26.7
OC	5.73	6.43	5.77	6.09	5.38
BC	0.47	0.46	0.49	0.53	6.67
$PM_{2.5}$	9.65	12.46	8.29	8.29	20.3

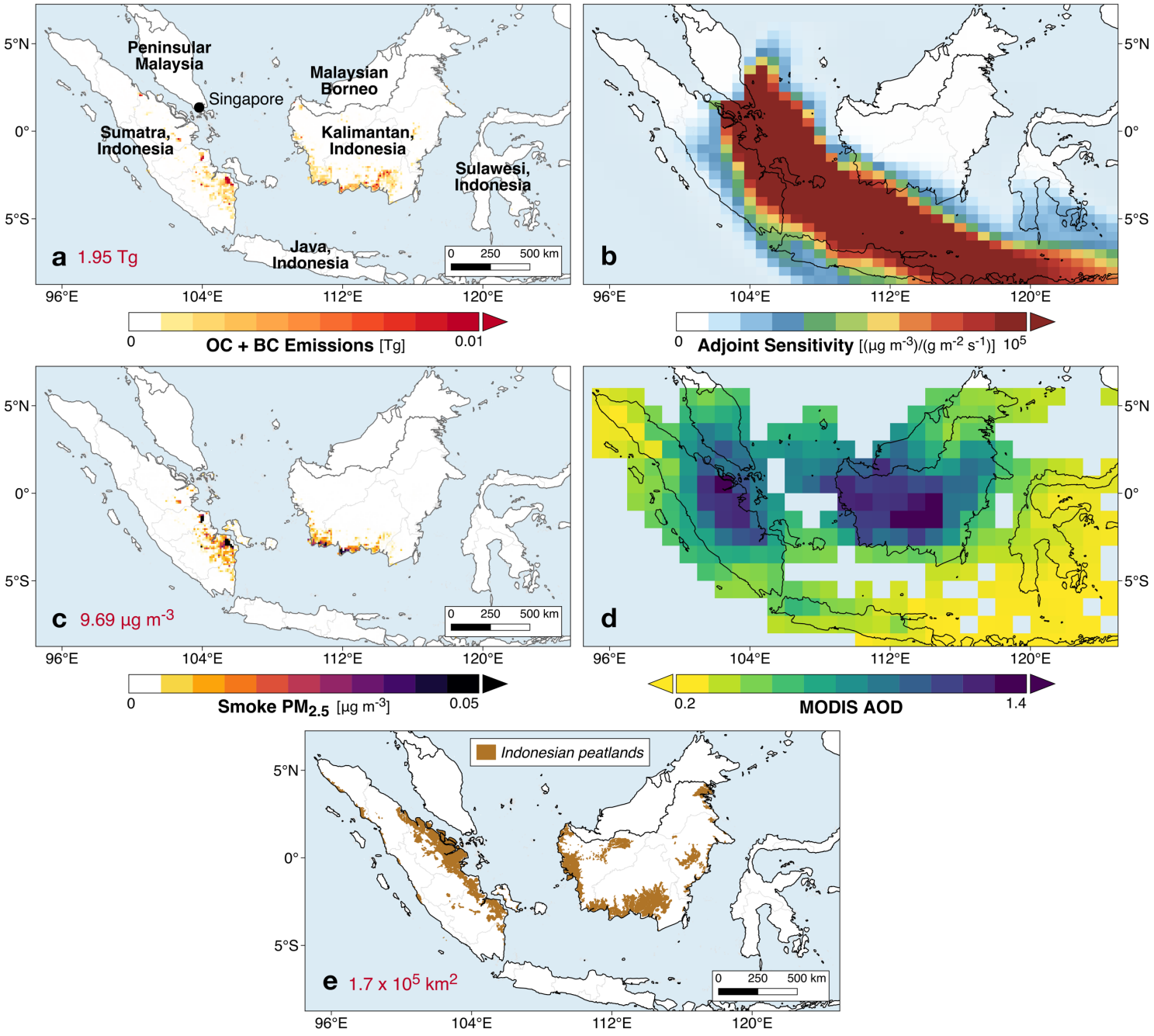

Figure 7. Indonesia fires, smoke exposure in Singapore, and AOD in Equatorial Asia during July-October in 2006. (**a**) Total organic carbon (OC) and black carbon (BC) emissions from GFASv1.2. Sum of OC+BC fire emissions over Indonesia is shown inset. (**b**) Sensitivity of mean July-October smoke concentrations in Singapore to the location of fire emissions, calculated by the GEOS-Chem adjoint. (**c**) Contribution of smoke $PM_{2.5}$ in Singapore from fires in individual grid cells over Indonesia, modeled using GFASv1.2 fire emissions. Average, calculated smoke $PM_{2.5}$ exposure in Singapore, which is the sum of these contributions, is shown inset. (**d**) Average MODIS Terra and Aqua aerosol optical depth (AOD) in Equatorial Asia. (**e**) Distribution of peatlands in Sumatra and Kalimantan, Indonesia. The approximate total peatland area in these regions is shown inset.

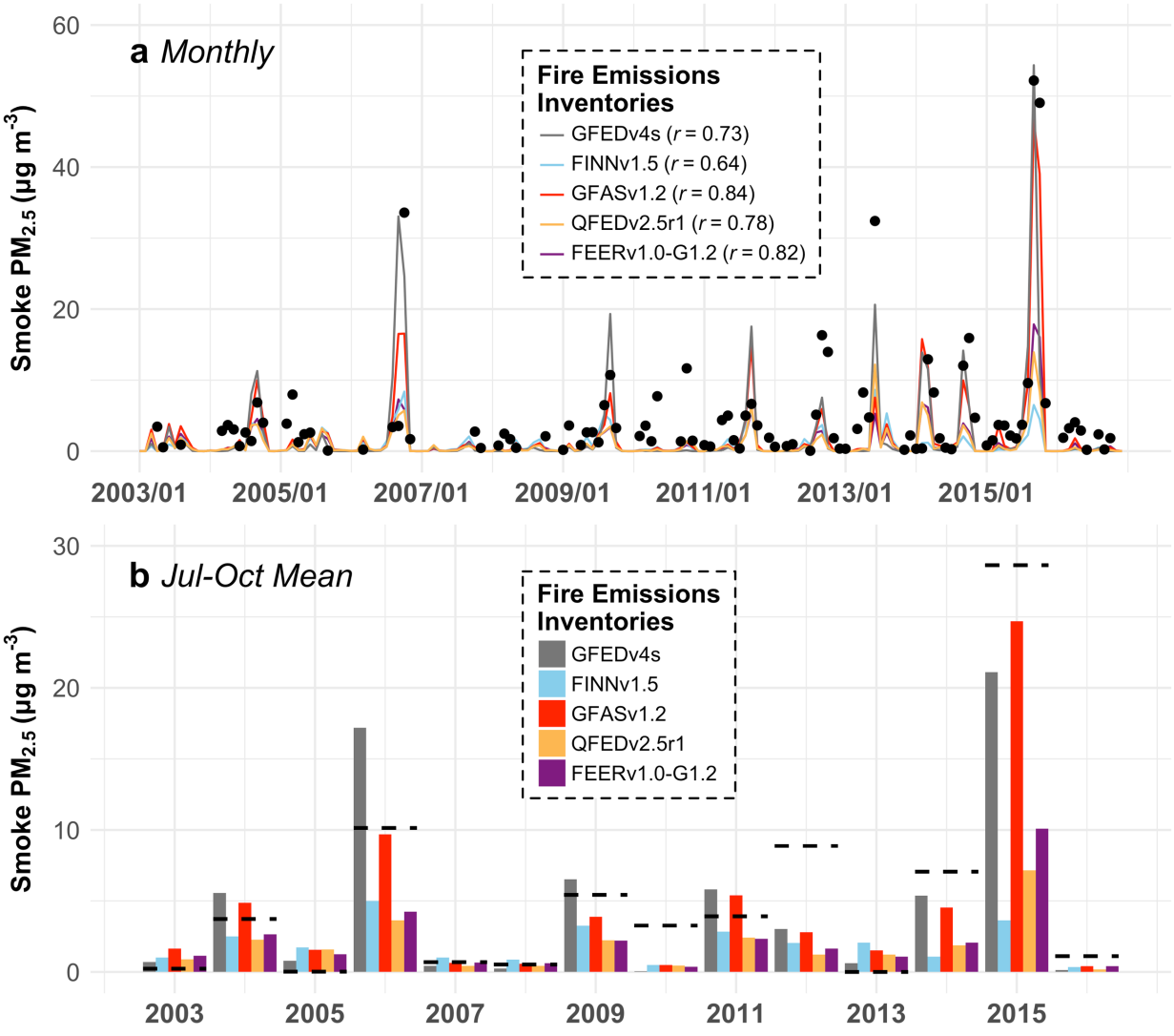

Figure 8. Smoke $PM_{2.5}$ exposure in Singapore, from 2003-2016. (**a**) Timeseries of monthly mean observed (black dots) and modeled (colored lines) smoke $PM_{2.5}$ concentrations. Observed smoke $PM_{2.5}$ is reconstructed from meteorological observations from the Singapore Changi Airport; only non-zero monthly smoke $PM_{2.5}$ observations are shown. Modeled values are from the GEOS-Chem adjoint using different global fire emissions inventories: GFEDv4s, FINNv1.5, GFASv1.2, QFEDv2.5r1, and FEERv1.0-G1.2. Correlations between observed and modeled smoke $PM_{2.5}$ are shown inset for each inventory and are statistically significant ($p < 0.01$). (**b**) Jul-Oct mean smoke $PM_{2.5}$ by inventory, with observed smoke $PM_{2.5}$ indicated by dashed horizontal lines.

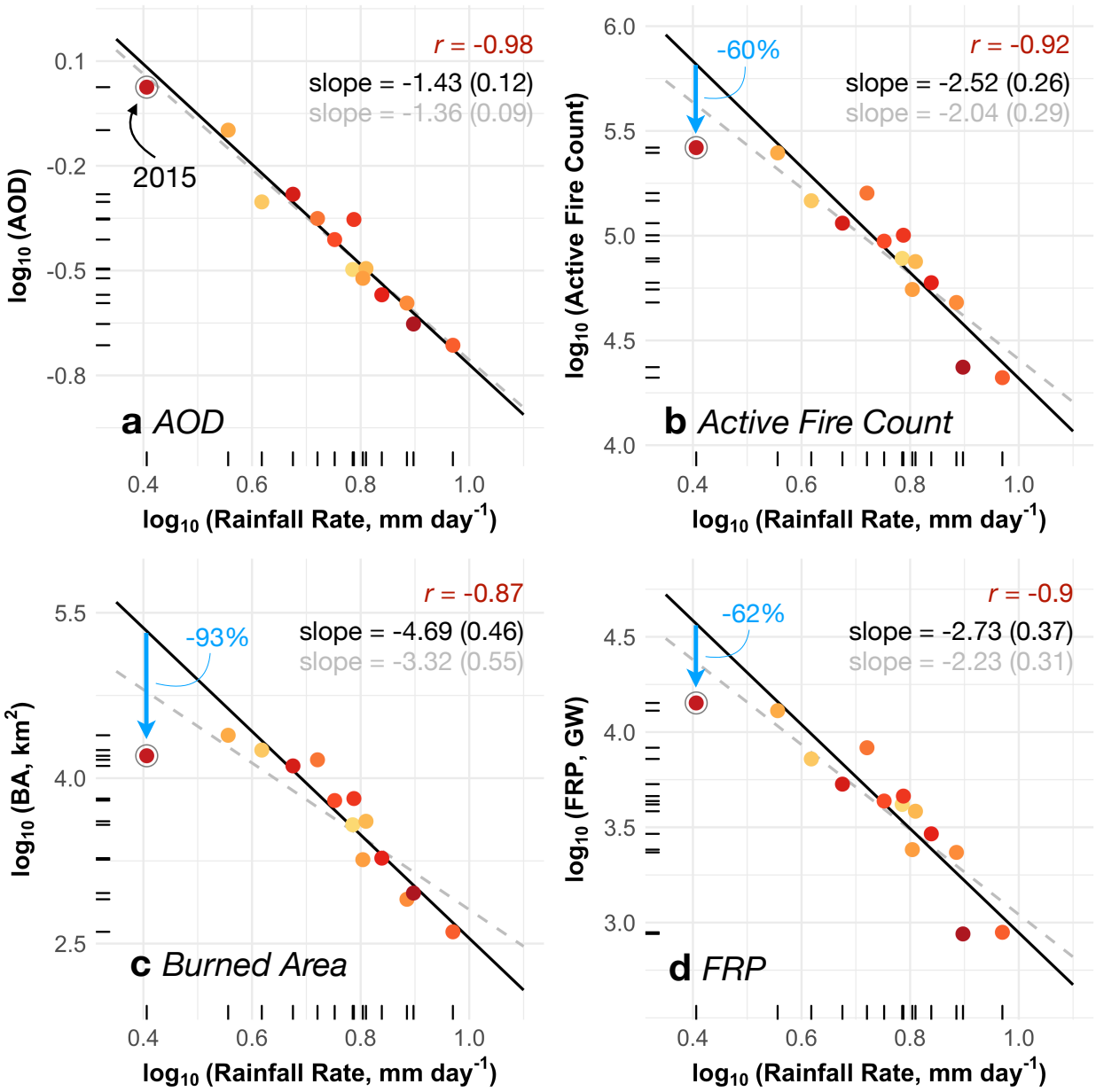

Figure 9. Under-detection of 2015 Indonesia fires in MODIS active fire and burned area products relative to the 2003-2016 period. CHIRPS rainfall rates (mm day^{-1}) are plotted against MODIS (**a**) aerosol optical depth, (**b**) active fire count, (**c**) burned area (km^2), and (**d**) FRP (GW) in log-log space. All variables are averaged temporally over July-October and spatially over Sumatra and Kalimantan, Indonesia. Colors denote different years from 2003-2016, with later years depicted by redder shades; values for 2015 are circled. Inset shows the correlation (r, $p <$ 0.01), slope of the linear regression (gray dashed line), and slope with 2015 removed (black line) for each pair of observations. Standard errors for the slopes are shown in parentheses. There is no statistically significant linear trend in any variable over time. Blue arrows in (**b**), (**c**), and (**d**) show that observed fires are lower than expected based on prediction from the linear regression of rainfall and fires that excludes 2015 observations. Percent underestimate of each fire variable based on these predictions is shown in blue.